Multi-material Eulerian Formulations and Hydrocode for the Simulation of Explosions

Ma Tianbao[1], Wang Cheng and Ning Jianguo

Abstract: A multi-material Eulerian hydrodynamic numerical method and hydrocode that can effectively simulate explosion problems in engineering practice were developed in this study. A modified Youngs' interface reconstruction algorithm was proposed for mixed cells, in which the material's volume fractions of the surrounding cells are not only used to reconstruct the material interface but also adopted to determine the transport order of the material. The algorithm developed herein was validated by the modeling of several tests, such as objects with different shapes moving in translational, rotating and shear flow field in two dimensional Descartes coordinates and axis-symmetric cylindrical coordinates. Results show that convergence is indeed obtained. Moreover, the explosion problem in the tunnel with an expansion-chamber and the jet formation of shaped charge were numerically simulated, and the numerical results show good agreement with the observed experimental data.

Keyword: Eulerian method, finite difference, numerical simulation, Youngs' algorithm, explosion problem, shaped charge jet.

1 Introduction

There are many explosion phenomena in engineering practice, such as explosion machining, shaped charge jets in oil well perforators in the oil industry, evaluation of explosion accidents in buildings or underground tunnels. Besides theoretical and experimental approaches, numerical simulations begin to play an important role in studying these phenomena with the rapid progress in computer software and numerical methods. The commonly used methods for these large distortion problems are Eulerian method and meshless method [Arefmanesh, Najafi and Abdi(2008); Moulinec, Issa, Marongiu and Violeau (2008); Mohammadi (2008); Han, Liu, Rajendran and Atluri (2006)].

---

[1] State Key Laboratory of Explosion Science and Technology, Beijing Institute of Technology, Beijing, P.R.C

In this paper, a two dimensional Eulerian finite difference method and hydrocode were developed for solving multi-material elastic-plastic hydrodynamic and in particular explosion problems. A modified Young's interface reconstruction algorithm was proposed for mixed cells. In this algorithm, the volume fractions of material of surrounding cells are used not only to reconstruct the material interface but also to determine the transport order of materials. To test the numerical precision of the modified Young's interface reconstruction algorithm, movements of objects with a variety of shapes in translational, rotating, and shear flow fields were numerically simulated in two dimensional Descartes as well as axis-symmetric cylindrical coordinate. In addition, as a test, the explosion field of tunnel with expansion-chamber and the jet formation of shaped charge were also numerically simulated.

2 Governing Equations

2.1 Conservation Equations

To simplify the computational model, materials studied here are assumed to be an isotropic and uniform continuum with ideal plasticity and in local thermodynamic equilibrium. Only small deformations are considered here.

Under such assumptions, the mass, momentum and energy conservation equations are as follows [Ning, Wang and Ma(2006); Ma and Ning(2005)],

$$\frac{\partial \rho}{\partial t} + \nabla \cdot (\rho \mathbf{u}) = 0 \tag{1}$$

$$\frac{\partial \rho \mathbf{u}}{\partial t} + \nabla \cdot (\rho \mathbf{u} \otimes \mathbf{u}) = \nabla \cdot \boldsymbol{\sigma} \tag{2}$$

$$\frac{\partial E}{\partial t} + \nabla \cdot (\rho E \mathbf{u}) = \boldsymbol{\sigma} : \dot{\boldsymbol{\varepsilon}} \tag{3}$$

These conservation equations can be rewritten as

$$\frac{\partial \rho}{\partial t} + \mathbf{u} \cdot \nabla \rho + \rho \nabla \cdot \mathbf{u} = 0 \tag{4}$$

$$\rho \left(\frac{\partial \mathbf{u}}{\partial t} + \mathbf{u} \cdot (\nabla \mathbf{u}) \right) = \nabla \cdot \boldsymbol{\sigma} \tag{5}$$

$$\rho \left(\frac{\partial e}{\partial t} + \mathbf{u} \cdot \nabla e \right) = \boldsymbol{\sigma} : \dot{\boldsymbol{\varepsilon}} \tag{6}$$

where t is time, $\boldsymbol{u}$ is the velocity, $\boldsymbol{\sigma}$ is the Cauchy stress tensor, $\dot{\boldsymbol{\varepsilon}}$ is the strain rate tensor, ρ is the density, E is the total specific energy, and e is the specific internal energy.

In two-dimensional axis-symmetric coordinates,

$$\frac{\partial \rho}{\partial t} + u_z \frac{\partial \rho}{\partial z} + u_r \frac{\partial \rho}{\partial r} + \rho \left(\frac{\partial u_z}{\partial z} + \frac{\partial r u_r}{r \partial r} \right) = 0 \tag{7}$$

$$\rho \left(\frac{\partial u_z}{\partial t} + u_z \frac{\partial u_z}{\partial z} + u_r \frac{\partial u_z}{\partial r} \right) = -\frac{\partial P}{\partial z} + \frac{\partial S_{zz}}{\partial z} + \frac{\partial (r S_{rz})}{r \partial r} \tag{8}$$

$$\rho \left(\frac{\partial u_r}{\partial t} + u_z \frac{\partial u_r}{\partial z} + u_r \frac{\partial u_r}{\partial r} \right) = -\frac{\partial P}{\partial r} + \frac{\partial S_{rz}}{\partial z} + \frac{\partial (r S_{rr})}{r \partial r} + \frac{S_{zz} + S_{rr}}{r} \tag{9}$$

$$\rho \left(\frac{\partial e}{\partial t} + u_z \frac{\partial e}{\partial z} + u_r \frac{\partial e}{\partial r} \right) = -P \left(\frac{\partial (r u_r)}{r \partial r} + \frac{\partial u_z}{\partial z} \right) + S_{zz} \frac{\partial u_z}{\partial z} + S_{rr} \frac{\partial u_r}{\partial r}$$
$$+ S_{rz} \left(\frac{\partial u_z}{\partial r} + \frac{\partial u_r}{\partial z} \right) - \frac{u_r (S_{zz} + S_{rr})}{r} \tag{10}$$

where r and z are the radial and axial coordinate of the cylindrical coordinate system, respectively; u_r and u_z are the radial and axial component of velocity; S_{rr}, S_{zz}, S_{rz} are components of stress deviator tensor.

2.2   Constitutive Relation

Within the range of small deformations, deviatoric stresses follow the general Hooke's law,

$$\overset{\triangledown}{\mathbf{S}} = \dot{\mathbf{S}} + \Omega \cdot \mathbf{S} - \mathbf{S} \cdot \Omega$$
$$= 2G[\dot{\boldsymbol{\varepsilon}} - (\mathrm{tr}\dot{\boldsymbol{\varepsilon}})\mathbf{I}] + \Omega \cdot \mathbf{S} - \mathbf{S} \cdot \Omega \tag{11}$$

where, the strain rate tensor and spin rate tensor are

$$\dot{\boldsymbol{\varepsilon}} = \frac{1}{2} (\mathbf{u}\nabla + \nabla\mathbf{u}) \tag{12}$$

$$\Omega = \frac{1}{2} (\mathbf{u}\nabla - \nabla\mathbf{u}) \tag{13}$$

in two-dimensional axis-symmetric coordinates,

$$\dot{S}_{rr} = 2G \left(\dot{\varepsilon}_{rr} - \frac{1}{3}D \right) - 2R' S_{rz} \tag{14}$$

$$\dot{S}_{zz} = 2G \left(\dot{\varepsilon}_{zz} - \frac{1}{3}D \right) - 2R' S_{rz} \tag{15}$$

$$\dot{S}_{rz} = 2G\dot{\varepsilon}_{rz} + R'(S_{zz} - S_{rr}) \tag{16}$$

where G is the shear modulus of elasticity; $\dot{\varepsilon}_{rr}$, $\dot{\varepsilon}_{zz}$ and $\dot{\varepsilon}_{rz}$ are components of strain rates. In the cylindrical coordinate, $\dot{\varepsilon}_{rr}$, $\dot{\varepsilon}_{zz}$, $\dot{\varepsilon}_{rz}$, D, and R' can be expressed as,

$$\dot{\varepsilon}_{rr} = \frac{\partial u_r}{\partial r} \tag{17}$$

$$\dot{\varepsilon}_{zz} = \frac{\partial u_z}{\partial z} \tag{18}$$

$$\dot{\varepsilon}_{rz} = \frac{1}{2}\left(\frac{\partial u_z}{\partial r} + \frac{\partial u_r}{\partial z}\right) \tag{19}$$

$$D = \frac{\partial(ru_r)}{r\partial r} + \frac{\partial u_z}{\partial z} \tag{20}$$

$$R' = \frac{1}{2}\left(\frac{\partial u_r}{\partial z} - \frac{\partial u_z}{\partial r}\right) \tag{21}$$

2.3 Yield Criterion

The plastic flow regime is determined by the von-Mises criterion in which the flow is considered as plastic when the second stress invariant J_2 exceeds the known flow stress Y_0. The individual deviators are then brought back to the flow surface,

$$S_{ij} = S_{ij}\sqrt{\frac{2Y_0^2}{3J_2}} \tag{22}$$

2.4 Equation of State

The equation of state can be expressed as follows

$$P = P(\rho, e) \tag{23}$$

Some typical equations of state such as JWL, Mie-Grvneisen and so on have been incorporated into the hydrocode, which can be seen in Section 6 and Section 7.

2.5 Artificial Viscosity

An artificial viscosity is introduced to calculate shock waves and improve the stability of solutions:

$$q_r = \rho\left(|\Delta u_r| - \Delta u_r\right)\left(a_n\left(|\Delta u_r| - \Delta u_r\right) + b_n c\right) \tag{24}$$

$$q_z = \rho\left(|\Delta u_z| - \Delta u_z\right)\left(a_n\left(|\Delta u_z| - \Delta u_z\right) + b_n c\right) \tag{25}$$

where q_r and q_z are artificial viscosities in the r and z direction, respectively; a_n and b_n are the second-order and the first order artificial viscosity coefficient, respectively; c is the speed of sound; Δu_r is the velocity gradient in the r direction; Δu_z is the velocity gradient in the z-direction.

2.6 Determination of Time Step

To ensure the convergence of the scheme, the time step is selected so that it satisfies the CFL (Courant-Friedrichs-Lewy) condition

$$\Delta t^n = \alpha_0 \cdot \min \left[\frac{\Delta z_i}{u_{zi,j}^n + c}, \frac{\Delta r_j}{u_{ri,j}^n + c} \right], \quad 0 < \alpha_0 < 1 \tag{26}$$

3 Numerical Method

3.1 Eulerian mesh

In the cylindrical coordinate, the computational domain is discrete into cylindrical meshes. Except for the artificial viscosity whose value is taken at the midpoint of cell edge, all other physical quantities, such as pressure, density, specific internal energy, velocity, and deviatoric stresses, are represented by their values at the cell center.
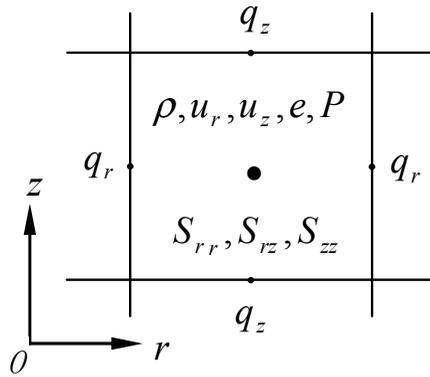

Figure 1: Definition of physical quantities

3.2 Lagrangian and advection computation

The conservation equations have the general form

$$\frac{\partial \boldsymbol{\phi}}{\partial t} + \mathbf{u} \cdot \nabla \boldsymbol{\phi} = \mathbf{H} \tag{27}$$

where $\boldsymbol{\phi} = [\rho, \mathbf{u}, e]^T$, and $\mathbf{H}$ is the source term.

Like some explicit Eulerian hydrocodes, the operator splitting method is employed here in which the conservation laws are separated into Lagrangian and Eulerian equations,

$$\frac{\partial \boldsymbol{\phi}}{\partial t} = \mathbf{H} \tag{28}$$

$$\frac{\partial \boldsymbol{\phi}}{\partial t} + \mathbf{u} \cdot \nabla \boldsymbol{\phi} = 0 \tag{29}$$

Thus the calculation for each time step is divided into two steps. The first step is a Lagrangian step in which the mesh is allowed to distort with the material. It is in this step that the changes in velocity and internal energy due to pressure and deviatoric stresses are calculated. The Lagrangian equations are numerically integrated with time by using a first order accuracy finite difference scheme, and changes in both axial and radial direction are calculated simultaneously,

$$\begin{aligned}
\tilde{\boldsymbol{\phi}}^{n+1} =& \boldsymbol{\phi}^n + \frac{\Delta t}{\Delta z} \left(\mathbf{H}^n_{i+1/2,j} - \mathbf{H}^n_{i-1/2,j} \right) \\
& + \frac{\Delta t}{\Delta r} \left(\mathbf{H}^n_{i,j+1/2} - \mathbf{H}^n_{i,j-1/2} \right)
\end{aligned} \tag{30}$$

Substituting $\tilde{\mathbf{u}}^{n+1}$ to Eq.29, the following equation is obtained:

$$\boldsymbol{\phi}^{n+1} = \tilde{\boldsymbol{\phi}}^{n+1} - \Delta t \, \tilde{\mathbf{u}}^{n+1} \cdot \nabla \tilde{\boldsymbol{\phi}} \tag{31}$$

Generally speaking, the solve of Eq.31 is accomplished by moving material across cell edges, in which the appropriate amounts of volume, mass, momentum, and internal energy are transported between the cells. So this step is usually called transport step. This may be thought of as remapping the distorted mesh at the end of step 1 back to the original fixed Eulerian frame. Because the remap differential equations Eq.29 are multidimensional and difficult to solve, they are simplified by being transformed to a set of one-dimensional equations using operator splitting method.

At first, the volume flux between cells is calculated. All of the materials to the right of the dotted line in Fig.2 will cross the right-hand edge during this step. The volume flux for edge $(i, j+1/2)$ is given by

$$F_{i,j+1/2} = \Delta t u_{i,j+1/2} \cdot A_{i,j+1/2} \tag{32}$$

where u is the velocity vector and A is cell edge area vector. Then interface tracking algorithm or interface reconstruction algorithm decides which materials in the

donor cell are moved with the volume and each material's volume flux. After the transport of material θ in the r direction is performed, the intermediate value of its volume fraction is given by

$$\tilde{f}_\theta = \left(f_\theta^n V_{i,j} + F_{\theta i,j-1/2} - F_{\theta i,j+1/2} \right) / V_{i,j} \tag{33}$$

in which V_{ij} is the volume of the (i, j)th cell; f is the volume fraction of material θ at time step n; F is the volume flux of material θ across the cell edges.

Figure 2: Volume flux in advection step

Then the material interface reconstruction algorithm is used again to determine the new interface location using the value $\tilde{f}_\theta$. And through the transport in the z-direction, the volume fraction of material θ at time step n+1 is finally calculated.

$$f_\theta^{n+1} = \left(\tilde{f}_\theta V_{i,j} + F_{\theta i-1/2,j} - F_{\theta i+1/2,j} \right) / V_{i,j} \tag{34}$$

Finally, the mass, momentum and internal energy of each material are moved between cells. To improve the accuracy, a second order conservative van Leer remap scheme[Van, L. B. (1997)] is adopted, in which a uniform distribution in the donor cell is replaced with a linear distribution. This scheme drastically reduces numerical dispersions and does not introduce spurious oscillations common to other higher order schemes.

In the advection or remap step, it is difficult to calculate advection for multi-material mixed cells. Interface reconstruction techniques have to be used to dynamically construct material interfaces within mixed cells. This will be discussed in the next section.

4   Calculation of Multi-Material Interface

The Eulerian method, for its advantages in simulating flows with large distortions, has been widely used in simulating explosion problems. However, when more than one material is present in the donor cell, the Eulerian method is difficult to identify material interfaces. Thus, interface reconstruction algorithms are required. Many algorithms have been successfully developed such as cell-type[Hardlow and Welch (1965); Gentry, Martin and Daly (1966)], VOF (volume of fluid) [Hirt and Nichols (1981)], and Level Set method[Sethian and Strain (1992)]. Among them, the VOF method, which includes SLIC (simple line interface calculation)[Noh and Woodward (1976)] and Youngs' interface reconstruction method[Youngs (1982)], is widely adopted in many Eulerian hydrocodes. W. J. Rider [Rider and Kothe (1998)] summarized the salient features of notable interface reconstruction and volume advection algorithms.

The second order Youngs' interface reconstruction algorithm is efficient for its simplicity and robustness. The basic idea is to replace the real material interface by a straight line as shown in Fig.3, then to determine the normal to the straight line based on the volume fractions of this and neighboring cells, and finally to adjust the position of straight line to match the volume fraction of the material. In a uniform mesh, Youngs uses equation (35) to calculate the slope [Pilliod (2004)].

$$\frac{\partial f}{\partial r} = \frac{f_E - f_W}{2\Delta r}, \quad \frac{\partial f}{\partial z} = \frac{f_N - f_S}{2\Delta z} \tag{35a}$$

$$k = -\frac{\partial f}{\partial r} \bigg/ \frac{\partial f}{\partial z} \tag{35b}$$

The variables f_E, f_W, f_N, and f_S shown in Fig. 4 are given by

$$\begin{aligned}
f_E &= \frac{f_{i-1,j+1} + \alpha f_{i,j+1} + f_{i+1,j+1}}{2+\alpha}, \\
f_W &= \frac{f_{i-1,j-1} + \alpha f_{i,j-1} + f_{i+1,j-1}}{2+\alpha} \\
f_N &= \frac{f_{i+1,j-1} + \alpha f_{i+1,j} + f_{i+1,j+1}}{2+\alpha}, \\
f_S &= \frac{f_{i-1,j-1} + \alpha f_{i-1,j} + f_{i-1,j+1}}{2+\alpha}
\end{aligned} \tag{35c}$$

where α is a free parameter. Parker and Youngs reported that $\alpha=2$ seemed to give the best results.

Youngs' algorithm only determines the location of material interfaces in mixed cells. It doesn't take into account the sequence of transported materials, which has

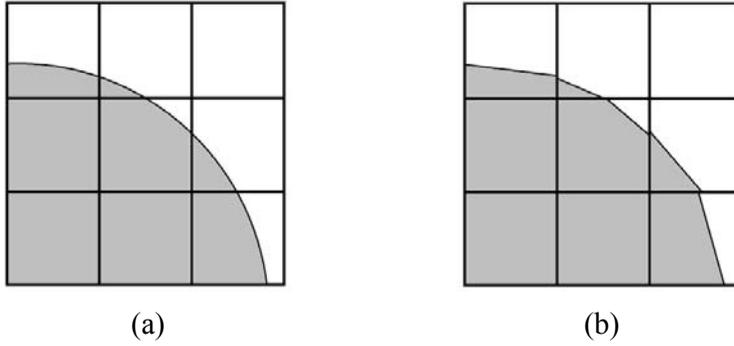(a)   (b)

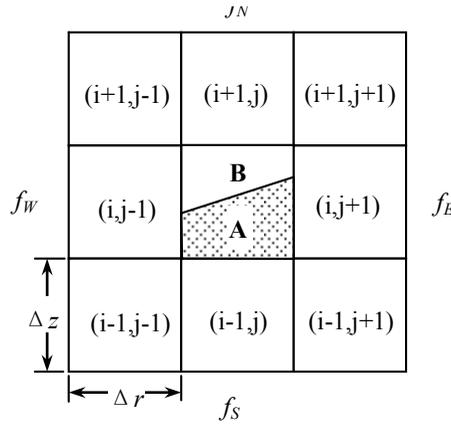Figure 3: Material interface reconstructed by Youngs' algorithm

Figure 4: Configuration of cells

to be addressed in the Eulerian method. Here we propose a criterion to determine the transportation sequence.

In this criterion, the material occupation number for material k in the cells to the left and right of the current cell, IL_k and IR_k, is assigned to 0 if material k is absent and 1 if it is present, respectively. Then the volume fraction of material k in the cells to the left and right of the current cell VL_k and VR_k is calculated, where $0 \leq VL_k \leq 1$, $0 \leq VR_k \leq 1$. Based on the values of IL_k, IR_k, VL_k and VR_k, the variables L_k and R_k are calculated by

$$L_k = IL_k \bullet Sgn(VR_k - VL_k) \tag{36}$$

$$R_k = IR_k \bullet Sgn(VR_k - VL_k) \tag{37}$$

Depending on all possible combinations of L_k and R_k, the distribution of material k can be categorized into five configurations as shown in Tab.1 and Fig.5.

Table 1: Configuration of materials

	L_k	R_k	configuration
1	0	1	a
2	1	1	b
3	-1	-1	c
4	-1	0	d
5	0	0	e

Once knowing the configuration of a specific material, its transportation priority can be determined based on the continuous principle. The transportation priority is a>b>c>d>e. For example, if species A belongs to the configuration b whereas species B belongs to the configuration c, the transport of species A is more preferentially considered than species B.

5   Numerical Tests

To test the resolution of the interface reconstruction algorithm proposed here, the movements of objects with various shapes in translational, rotating and shear flow field were investigated. The numerical verification was also performed to test the material interface tracking algorithm. In numerical calculations, the focus was placed onto verifying if the shape of objects keeps intact.

5.1   *Movement of a ring in a two dimensional translational flow in Descartes coordinates*

The size of computational region is 2×2, which is further divided into 200×200 rectangular Eulerian mesh. The length of time step is 0.001. The translational velocity field is given by $u_z(z,r) = u_r(z,r) = 1.0$.
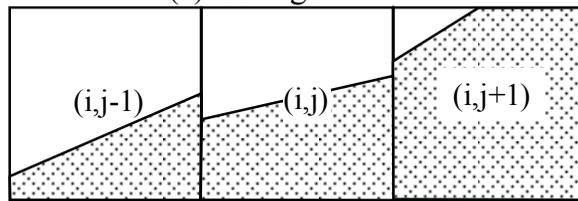
The snapshots of the ring at different time steps are shown in Fig.6 where n represents the number of time step. As shown, the shape as well as volume of the ring does not change during the motion.

5.2   *Movement of a semicircle in a two dimensional rotating flow in Descartes coordinates*
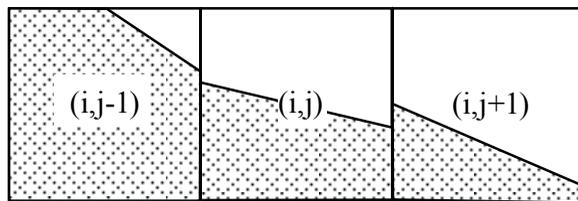
The size of computational region is $\pi \times \pi$, which is further divided into 200×200 rectangular Eulerian mesh. The length of time step is 0.001. The rotating velocity field is given by $u_z(z,r) = -\pi \cdot (r - \pi/2)$, $u_r(z,r) = \pi \cdot (z - \pi/2)$.
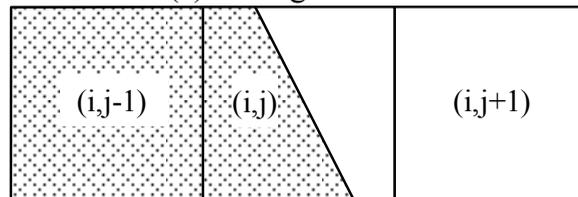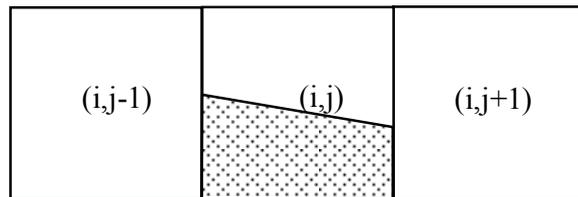
(a) Configuration a

(b) Configuration b

(c) Configuration c

(d) Configuration d

(e) Configuration e

Figure 5: Five material configurations of modified Youngs' algorithm
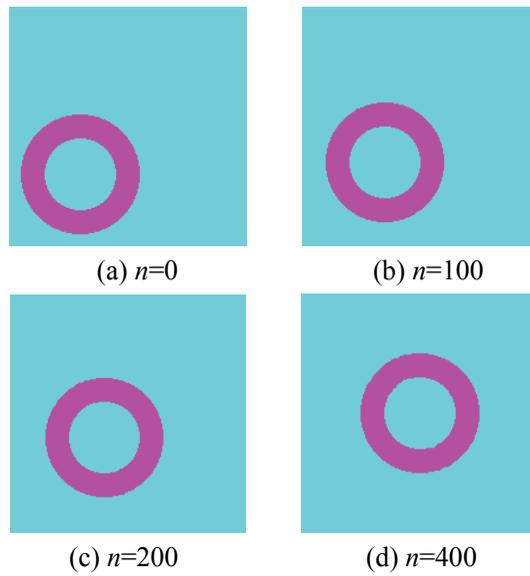
Figure 6: The snapshots of a ring in two dimensional translational velocity field at different time steps
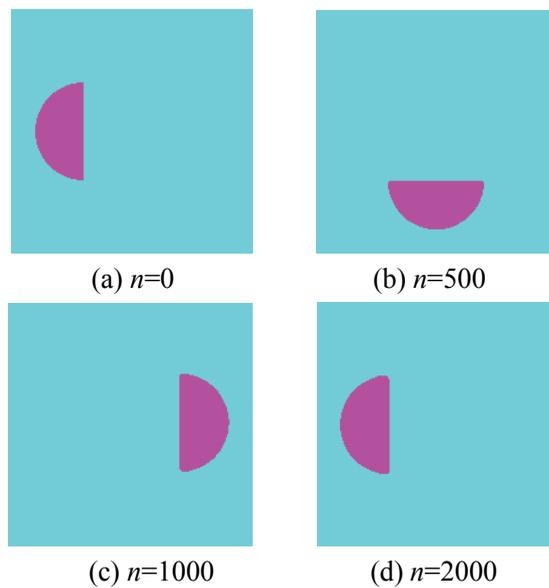

Figure 7: The snapshots of a semicircle in two dimensional rotating velocity field at different time steps

The snapshots of the semicircle are shown in Fig.7 at time step 0, 500, 1000, and 2000, respectively. It can be seen from the figure that, even through the shape of the semicircle keeps well during simulation; the shape changes more than the circle in Fig.6. Particularly, at the large time step, the edge of the semicircle becomes less smooth and its corner is less sharp too.

5.3 Movement of a Disk in a two dimensional shear flow in Descartes coordinates

The size of computational region is $\pi \times \pi$, which is further divided into 200×200 rectangular Eulerian mesh. The length of time step is 0.001. The shear flow is given by $u_z(z,r) = -\pi \cdot \sin z \cdot \cos r$; $u_r(z,r) = \pi \cdot \cos z \cdot \sin r$.

Taking them as initial values, calculation is performed until time step is n=1500, and then the state at time step n=1500 is treated as initial condition, calculation is reversely performed to time step n=3000 in order to test if the disk can be brought back to its initiation configuration, as indicated in Fig.8. It is noted that the disk can be back to its starting shape without any evident difference.
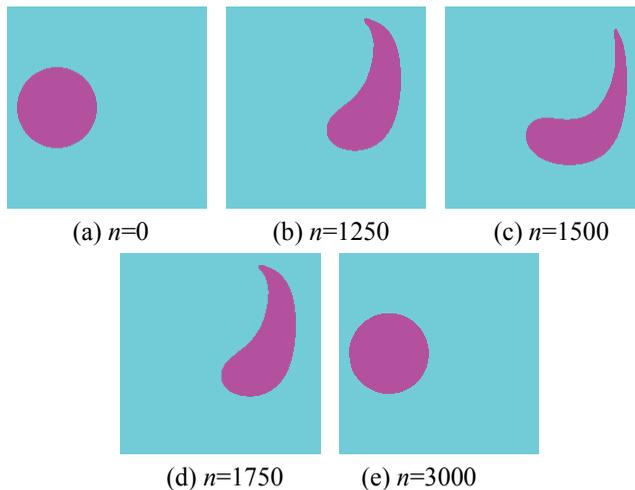

(a) *n*=0   (b) *n*=1250   (c) *n*=1500

(d) *n*=1750   (e) *n*=3000

Figure 8: The snapshots of a disk moving in a two dimensional the shear flow

5.4 Movement of objects with conical nose and ogive nose in an axis-symmetric translational flow

The size of computational region is 10×2, which is further divided into 500×100 rectangular Eulerian mesh. The length of time step is 0.001. The initial velocity at z and r direction is $u_{z0} = 1.0$ and $u_{r0} = 0.0$, respectively.
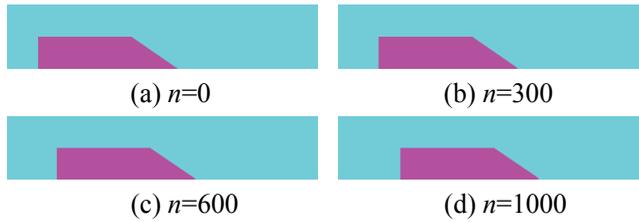
Figure 9: The snapshots of an object with conical nose in an axis-symmetric translational velocity field
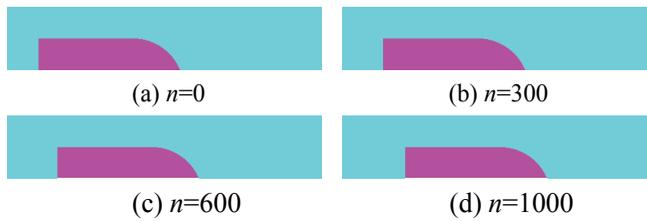

Figure 10: The snapshots of an object with ogive nose in an axis-symmetric translational velocity field

The snapshots of the objects with conical nose and ogive-nose are shown in Fig. 9 and Fig. 10, respectively. In both cases, the shape of the nose changes while the size and whole shape remain the same.

As shown in above examples, using the modified Youngs' interface reconstruction algorithm to describe the material interface in Eulerian hydrocode is feasible. The algorithm keeps the shape and volume of objects with either a curve or straight boundary in both Descartes and cylindrical coordinates pretty well.

6   Explosion Problem in Tunnel with Explosion-Chamber

In engineering practice, it is often required to evaluate the risk of explosion accidents and take the corresponding protection measures to alleviate the damage of buildings, engineering facilities and human beings from explosions. The shock wave interactions with barriers are crucial in the protection design of mines, tunnels, factories and so on. However, it is difficult to study these interactions in explosion experimentally, because explosion is usually occurred within a very short period and is very dangerous due to the high pressure and temperature. As a result, explosion is often studied by numerical simulation. To evaluate the efficiency of the proposed Eulerian method and hydrocode in the simulation of these problems,

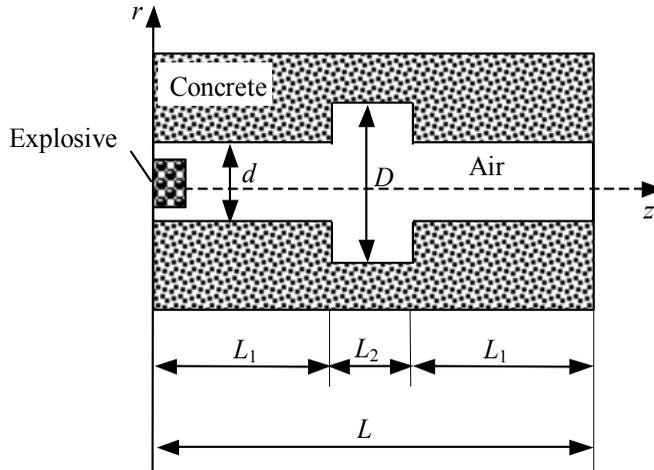the simulation of explosions in a tunnel was discussed.

Figure 11: The schematic representation of a tunnel with an expansion-chamber

The schematic representation of explosion field in a tunnel with an expansion-chamber is shown in Fig.11. The size of computational region is 25m×5.2m. The diameter of the tunnel is 2.5m. The mass of the explosive that placed on the entrance of the tunnel is 450kg. The computational region is divided into 500×104 rectangular Eulerian mesh. The length of the mesh is 0.05m.

In a tunnel with uniform section ($D = d$), the empirical attenuation law of shock wave over-pressure is,

$$\Delta P = 0.1692 \left(\frac{m}{SR}\right)^{\frac{1}{3}} + 0.0269 \left(\frac{m}{SR}\right)^{\frac{2}{3}} + 2.031 \left(\frac{m}{SR}\right) \tag{38}$$

where ΔP is the peak value of the over-pressure, m is the mass of the TNT explosive, S is the section area of the tunnel, and R is the distance to the explosion point.

The simulation results of shock waves propagation in uniform section tunnel are visualized[Zhang, Ning and Zheng (1999)] in Fig.12. Table 2 gives the over-pressure results from computation and empirical formula. It shows that the differences between the values from the two different methods are small and in the acceptable range.

To study the effects of expansion-chamber size on the attenuation of shock waves, explosions in tunnels with different expansion-chamber sizes were numerically simulated. The simulation results are visualized in Fig.13. In Fig.13, the reflection and disturbance of the shock wave in the expansion-chamber can be seen clearly.

Table 2: Attenuation of shock waves in a uniform section tunnel

R (m)	6	8	10	12	14	16
Empirical formula (MPa)	33.9	25	20.3	16.9	14.5	12.7
numerical results (MPa)	35.1	26.7	22.7	17.1	15.4	13.2

(a) n =100 t=0.16ms

(b) n =2000 t=2.16ms

(c) n =3000 t=3.8ms

(d) n =4000 t=5.85ms

Figure 12: Propagation of shock waves in uniform section tunnel

Furthermore, let P_2 and P_1 denote the pressure at the entrance of expansion-chamber and exit of expansion-chamber, respectively, the variation of ratio of P_2 to P_1 can be obtained. These results are summarized in Table 3. The following conclusions are drawn:

(1) When the length of the expansion-chamber is a constant, the pressure ratio of P_2 to P_1 decreases as the diameter of the tunnel increases. The reason is that, as its diameter increases, the tunnel produces more expansion disturbance to the shock waves and makes the energy of shock waves dissipate more quickly. Meanwhile, the propagation time of shock waves in the tunnel also increases

(a) $n=1100$ $t=1.19$ms

(b) $n=2600$ $t=3.0$ms

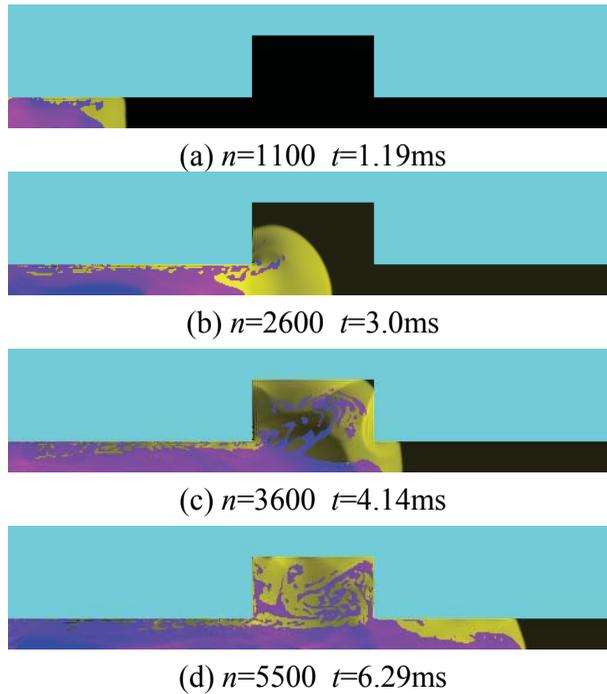(c) $n=3600$ $t=4.14$ms

(d) $n=5500$ $t=6.29$ms

Figure 13: Propagation of shock waves in the tunnel with expansion-chamber

with the diameter of expansion-chamber. For example, when $L_2 = 2d$, the propagation time of shock waves through the duct for $D = 2d$, $D = 3d$ and $D = 4d$ are 7.5ms, 7.7ms, 7.9ms, respectively.

(2) When the diameter of the expansion-chamber is a constant, the tunnel can weaken the shock waves more effectively as its length increases. The propagation time of shock waves in the tunnel also increases with the length of expansion-chamber. These conclusions provide valuable guidance for the design of expansion tube.

7   Calculations of Steel Shaped Charge Jet

As a test, the formation of shaped charge jet with conical angle of 70°/61.2° on the inside and outside surface of steel liner wall was numerically simulated. The schematic representation of experimental apparatus is shown in Fig.14. Three experimental results are averaged as the final experimental value [Wen (1998)].

Table 3: The variation of ratio of P_2 to P_1

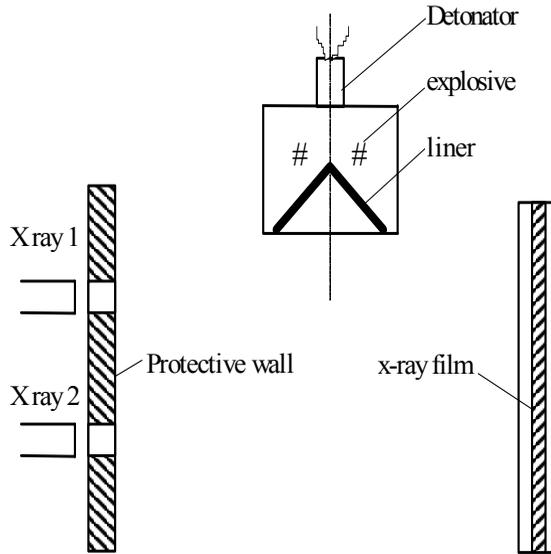| L_2	D		
	2d	3d	4d
1d	0.43	0.36	0.29
2d	0.35	0.34	0.27
3d	0.32	0.30	0.25
4d	0.29	0.28	0.23

Figure 14: Schematic representation of the experimental apparatus

High explosive detonation is simulated by a programmed burn model. The Jones-Wilkins-Lee (JWL) equation of state is adopted here, which is

$$P = A(1 - \frac{\omega}{R_1 V})\mathrm{e}^{-R_1 V} + B(1 - \frac{\omega}{R_2 V})\mathrm{e}^{-R_2 V} + \frac{\omega E}{V} \tag{39}$$

where A, B are linear coefficients used in JWL equation of state; R_1, R_2, ω are nonlinear coefficients used in JWL equation of state; E is specific internal energy per unit volume; V is the relative volume of explosive products. For the current study, B explosive is used as the main charge with parameters $A=3.712\times10^{11}$Pa, $B=3.231\times10^9$Pa, $R_1=4.15$, $R_2=0.95$, $\omega=0.30$, $E=7.0\times10^9$J·m^{-3}, $\rho=1600$kg·m^{-3}, $P_{CJ}=1.85\times10^{10}$Pa, $D_{CJ}=6900$m·s^{-1}. The diameter of the charge is 40mm, and the height is 41mm.
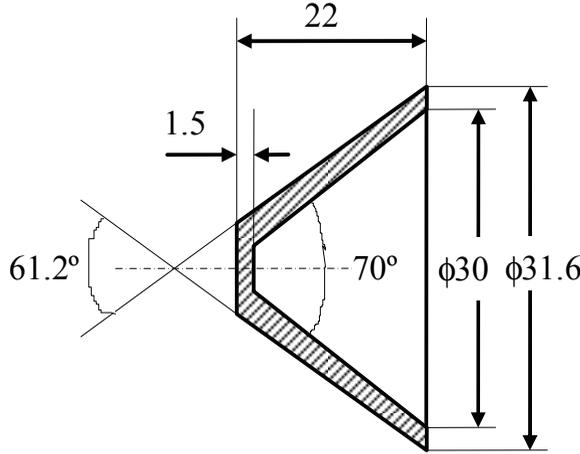
Figure 15: Geometric model of the liner

The ideal gas equation of state is used to describe air

$$P = (k-1)\rho \cdot e \tag{40}$$

where k is the ratio of specific heats.

The geometry of the steel liner is shown in Fig. 15. The Mie-Grneisen equation of state for metal can be expressed by

$$P = P_H \left(1 - \frac{\Gamma \mu}{2}\right) + \Gamma \rho \, (e - e_0) \tag{41}$$

and

$$P_H = \begin{cases} k_1 \mu + k_2 \mu^2 + k_3 \mu^3 & \mu \geq 0 \\ k_1 \mu & \mu < 0 \end{cases} \tag{42}$$

where Γ is Gruneisen constant, k_1, k_2 and k_3 are the known material constants.

The detonation of high explosive, the expansion of detonation products, the collapse of liner, and the jet formation are shown in Fig.16. These images show that the numerical method proposed in this paper can give better resolution of material interfaces.

As shown in Fig. 17, the maximum tip velocity reaches the value of 0.48cm/μs around t=12 μs and then slows down. At the time of 30.005μs, as shown in Table 4, the computed tip velocity is 0.4484cm/μs while the experimental value is
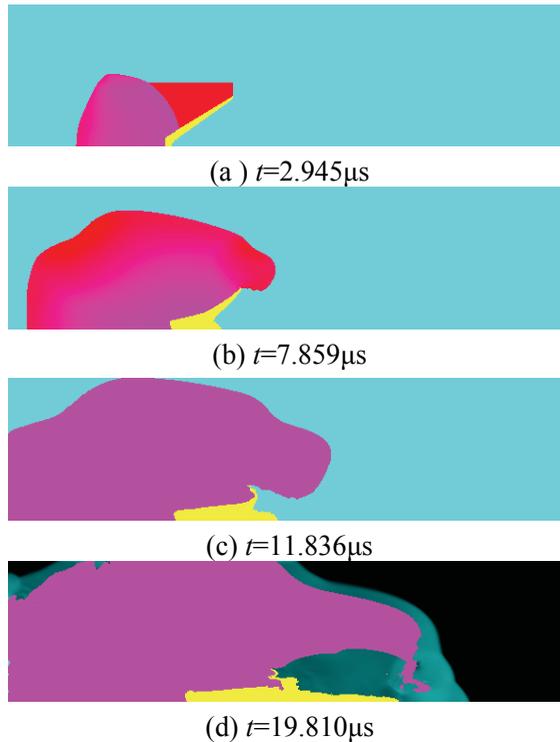
(a) t=2.945µs

(b) t=7.859µs

(c) t=11.836µs

(d) t=19.810µs

Figure 16: Jet formation of shaped charge

0.4625cm/µs. Similarly, the computed tail velocity is 0.1108cm/µs and is a little greater than the experimental value of 0.1010cm/µs.

The total length of the shaped charge jet as a function of time is shown in Fig.18. At time of 25.703µs, the length of the jet (the slug is not included) is 56.4mm, which is somehow shorter than the experimental value of 59.67mm.

The computational results as well as experimental values for the tip velocity, tail velocity and length, and diameter of the jet are summarized in Table 4. The computational results are in a good agreement with the experimental values, which indicates that the numerical method proposed in this paper is reasonable and useful for the optimization design of shaped charge jet.

The variation of collapse angles along the inside and the outside surfaces of the liner wall, β^{in} and β^{out}, are plotted in Fig. 20 as a function of time. It is helpful in the study of the formation process of the shaped charge jet
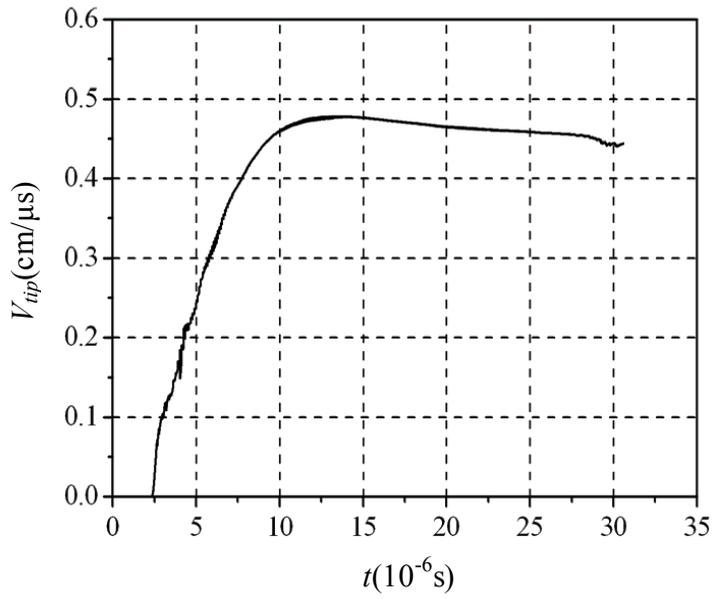
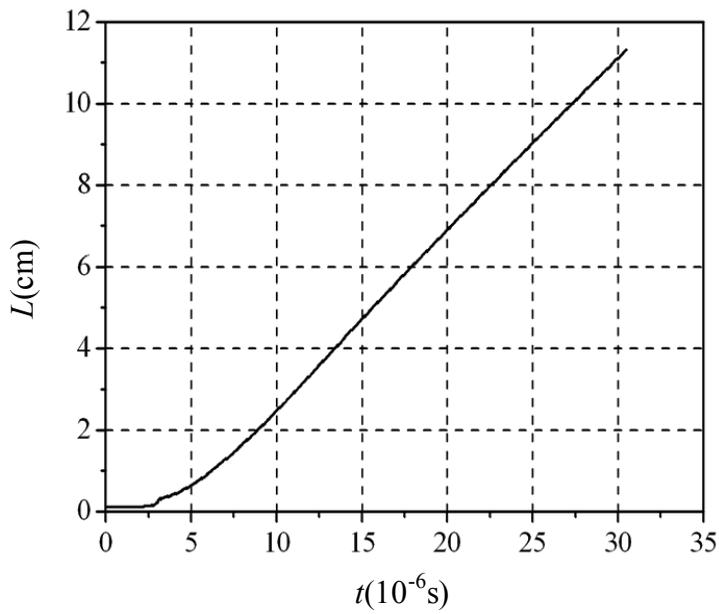Figure 17: Variations of tip velocity of the jet versus time

Figure 18: Variations of length of the jet versus time

Table 4: Comparison of experimental values to computed results

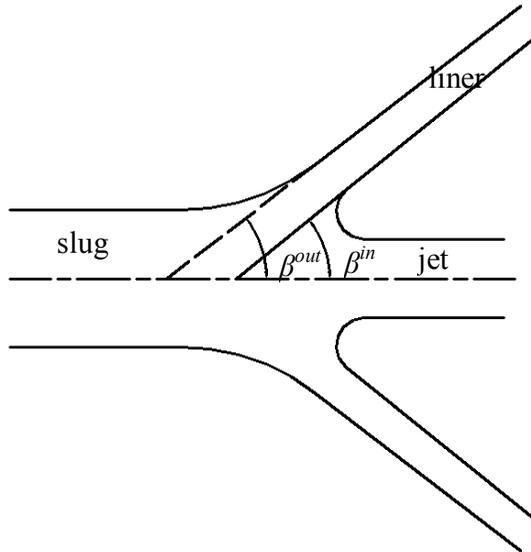|	Computed result	Experimental value	relative error
Tip velocity (cm/μs)	0.4484	0.4625	3.05%
Tail velocity (cm/μs)	0.1108	0.1010	9.70%
Length (mm)	56.4	59.67	5.48%
Diameter (mm)	2.6	2.23	16.59%

Figure 19: Schematic representation of collapse angles along the inside and outside surfaces of the liner wall

8   Conclusions

A multi-material Eulerian hydrodynamic numerical methods and modified Youngs' interface reconstruction algorithm were proposed in this study. Based on the above algorithm, the corresponding hydrocode was developed. Objects with a variety of shapes moving in different flow fields were numerically simulated to test the numerical precision of the proposed interface reconstruction algorithm. The explosion problem in the tunnel with an explosion-chamber and the jet formation of
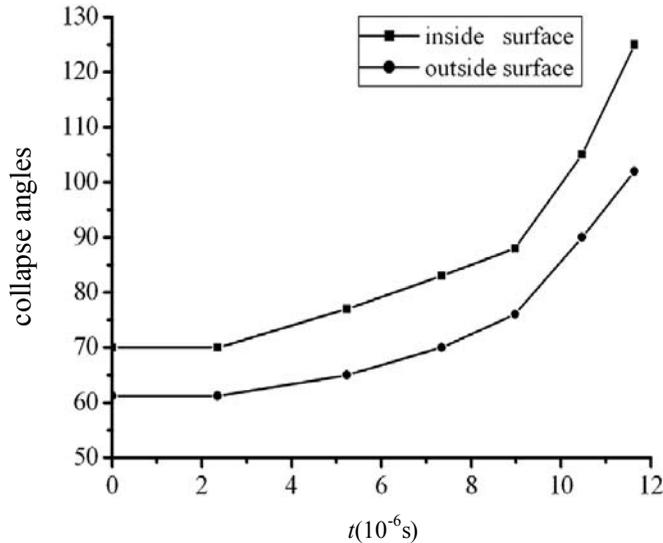
Figure 20: The variation of collapse angles along the inside and outside surfaces of the liner wall as a function of time

shaped charge were numerically simulated. The numerical results indicate that the numerical method and hydrocode proposed in this study is feasible and efficient for the simulation of engineering problems.

References

Arefmanesh, A.; Najafi, M.; Abdi, H. (2008): Meshless local Petrov-Galerkin method with unity test function for non-isothermal fluid flow. *CMES: Computer Modeling in Engineering & Sciences*, Vol. 25, No. 1, pp. 9-22.

Van, L. B. (1997): Towards the ultimate conservative difference scheme IV: A new approach to numerical convection. *J Comput Physics*, vol. 23, pp. 276-299.

Gentry, R. A.; Martin, R. E.; Daly, B. J. (1966): An Eulerian Differencing Method for Unsteady Compressible Flow Problems. *J Comput Physics*, vol. 1, pp. 87-118.

Han, Z. D.; Liu, H. T.; Rajendran, A. M.; Atluri, S. N. (2006): The applications of meshless local Petrov-Galerkin (MLPG) approaches in high-speed impact, pen-

etration and perforation problems. *CMES: Computer Modeling in Engineering & Sciences*, Vol. 14, No. 2, pp. 119-128.

Hardlow, F. H.; Welch, J. E. (1965): Numerical Calculation of Time Dependent Viscous Incompressible Flow of Fluid with Free Surface. *Phys. Fluids*, 1965, vol. 8, pp. 21∼82.

Hirt, C. W.; Nichols, B. D. (1981): Volume of Fluid (VOF) Method for the Dynamics of Free Boundaries. *J Comput Physics*, vol. 39, pp. 201-225.

Ma T. B.; Ning J. G. (2005): Numerical Simulation of Spherical Charge Exploding in Soil Medium. In: Feng, C. G. (ed) *Theory and Practice of Energetic Materials*, Vol. VI, Science Press, Beijing, pp. 964-969.

Mohammadi, M. H. (2008): Stabilized meshless local Petrov-Galerkin (MLPG) method for incompressible viscous fluid flows. *CMES: Computer Modeling in Engineering & Sciences*, Vol. 29, No. 2, pp. 75-94.

Moulinec, C.; Issa, R.; Marongiu, J. C.; Violeau, D. (2008): Parallel 3-D SPH simulations. *CMES: Computer Modeling in Engineering & Sciences*, Vol. 25, No. 3, pp. 133-148.

Ning, J. G.; Wang, C.; Ma, T. B. (2006): Numerical Analysis of the Shaped Charged Jet with Large Cone Angle. *International Journal of Nonlinear Sciences and Numerical Simulation*, Vol. 7, No. 1, pp. 71-78.

Noh, W. F.; Woodward, P. (1976): SLIC (Simple Line Interface Calculation). *Proc. of the fifth International Conference on Numerical Methods in Fluid Dynamics, Springer Lecture Notes in Physics, 59*, pp. 330-340.

Pilliod, J. E. (2004): Elbridge Gerry Puckett. Second-order accurate volume-of-fluid algorithms for tracking material interfaces. *J Comput Physics*, vol. 199, pp. 465-502.

Rider, W. J.; Kothe D. B. (1998): Reconstructing Volume Tracking. *J Comput Physics*, vol. 141, pp. 112-152.

Sethian, J. A.; Strain, J. (1992): Crystal growth and dendritic solidification. *J Comput Physics*, vol. 98, pp. 231.

Wen, W. Z. (1998): Marker on Cell Line (MOCL) and It's Application in Numerical Simulations. Doctoral thesis, Beijing Institute of Technology.

Youngs, D. L. (1982): Time-Dependent Multi-Material Flow with Large Fluid Distortion. In: Morton, K. W. and Baines, M. J. (ed) *Numerical Methods for Fluid Dynamics*, Academic Press, New York, pp. 273-285.

Zhang, W. Y.; Ning, J. G.; Zheng, Z. G. (1999): Visualization of explosive field. *Journal of Beijing Institute of Technology (English Edition)*, Vol. 8, No. 4, pp. 424-429.